DLR-IB-AS-BS-2022-62

RANS Investigations of Vortex Separated Flows

V. Togiti, A. Krumbein
Institute of Aerodynamics and Flow Technology
$C^2A^2S^2E$

Deutsches Zentrum
DLR für Luft- und Raumfahrt

Bericht des Instituts für Aerodynamik und Strömungstechnik
Report of the Institute of Aerodynamics and Flow Technology

DLR-IB-AS-BS-2022-62

RANS Investigations of Vortex Separated Flows

V. Togiti, A. Krumbein

Herausgeber:
Deutsches Zentrum für Luft- und Raumfahrt e.V.
Institut für Aerodynamik und Strömungstechnik
Lilienthalplatz 7, 38108 Braunschweig

ISSN 1614-7790

Stufe der Zugänglichkeit: 1
Braunschweig, im Juli 2022

Institutsdirektor:
Prof. Dr.-Ing. habil. C.-C. Rossow

Verfasser:
V. Togiti, A. Krumbein

Abteilung: C2A2S2E
Abteilungsleiter:
Prof.Dr. S. Görtz

Der Bericht enthält:
35 Seiten
25 Bilder
1 Tabellen
15 Literaturstellen

Contents

1. Introduction

Significant enhancements in computational fluid dynamics (CFD) have led to the use of numerical simulation in the design process of both civil and military aircraft, especially for nominal cruise performance where flows are generally characterized by attached flows. However, military vehicles routinely operate well outside of the steady, attached flow regimes often dominated by separated vortex flows. Therefore, major effort has to be devoted to ensure the vehicle qualified at many states that contain unsteady, highly separated flows. State-of-the-art CFD methods lack the ability to predict onset and progression of separated vortex-dominated flows, especially from smooth surfaces. Investigations carried out in several AVT task groups of the NATO Science and Technology Organization (STO) [1] indicate that the shortcomings for these predictions mainly stem from deficiencies of the models of turbulence. In most numerical investigations for slender wings with low sweep angle and blunt leading edges [2] linear eddy-viscosity turbulence models are employed. These models tend to deliver acceptable predictions at moderate incidence angles. However, at higher incidence angles, force coefficients and pitching moments were observed to be off compared to experiments. This is due to incorrect (earlier or delayed) prediction of incipient separation and differences in the strength of the subsequent development of vortices.

The linear eddy-viscosity models (EVM) are still the backbone of numerical simulations for industrial applications due to their numerical robustness. While being fairly reliable for attached boundary-layer flows, they often tend to fail in the case of flow separation. Furthermore, they are known to dissipate vortices too rapidly. The reason for the above failures of EVMs can be attributed to the underlying Boussinesq hypothesis, assuming the Reynolds stresses being parallel to the strain rate tensor, and to the discretized numerical representation of the Reynolds stresses in a code. Furthermore, the production terms of the underlying transport equations for the turbulent quantities need modeling. In contrast to EVMs full differential Reynolds stress models (RSM) provide individual transport equations for the Reynolds stresses. Its terms also have to be modeled, except for the production term which is treated exactly. For this reason, differential Reynolds stress models are considered particularly suitable for vortex-dominated flows. Investigations conducted in [3] [4] demonstrate the applicability of RSM for vortex dominated flows.

In this work, the objective is to demonstrate the capabilities of RSM over EVMs for the flows involving separation from a smooth body and the subsequent formation of vortices. To this end, investigations for the flow over a spheroid, a delta wing and a so-called diamond wing are carried out using RSM and the predictions are compared to the predictions of EMVs and experimental data.

2. Details of Investigated Configurations

In the current study the flows over a spheroid, a delta wing, and a diamond wing are investigated. These configurations unveil separation from a smooth surface and subsequent vortex formation. The flow over a spheroid at high incidence exhibits a three-dimensional cross flow separation and subsequent formation of longitudinal vortices, see Figure 1(a). Strength and location of these vortices determine the maneuver characteristics of the body. Therefore, the accurate prediction of flow separation and vortex strength are of the greatest importance to determine forces and moments exerted on the body. In the present work, the flow over a 6:1 prolate spheroid is investigated at a Reynolds number based on the streamwise length of the spheroid, L, of Re_L = $4.2x10^6$ and a Mach number of 0.2 at the incidence of α = 20°, based on the experimental investigations of [5]. As in the experiments, transition is set at x/L = 0.2 on both windward and leeward sides of the spheroid.

The other case investigated is the flow over the delta wing based on the experimental investigations carried out in the Vortex Flow Experiment-2 [6] at the DLR Göttingen. In the experiments, a 65° swept delta wing configuration with different rounded and sharp leading edges at angles of attack of 13.3 ° and 18 ° was investigated. In the experiments at the former incidence angle a partially developed separated vortex flow was observed while at the latter incidence angle a fully developed separated vortex flow was observed. In the current study the partially developed separated vortex flow case at a freestream Reynolds number based on the mean aerodynamic chord (c_{mac}) of $3x10^6$ and Mach number of 0.4 and the incidence angle of 13.3 ° with a medium radius rounded leading edge of r/c_{mac} = 0.15% is investigated. The flow topology at the aforementioned incidence angle is displayed in Figure *1* (b) which unveils vortex separation, inner and outer primary vortices.

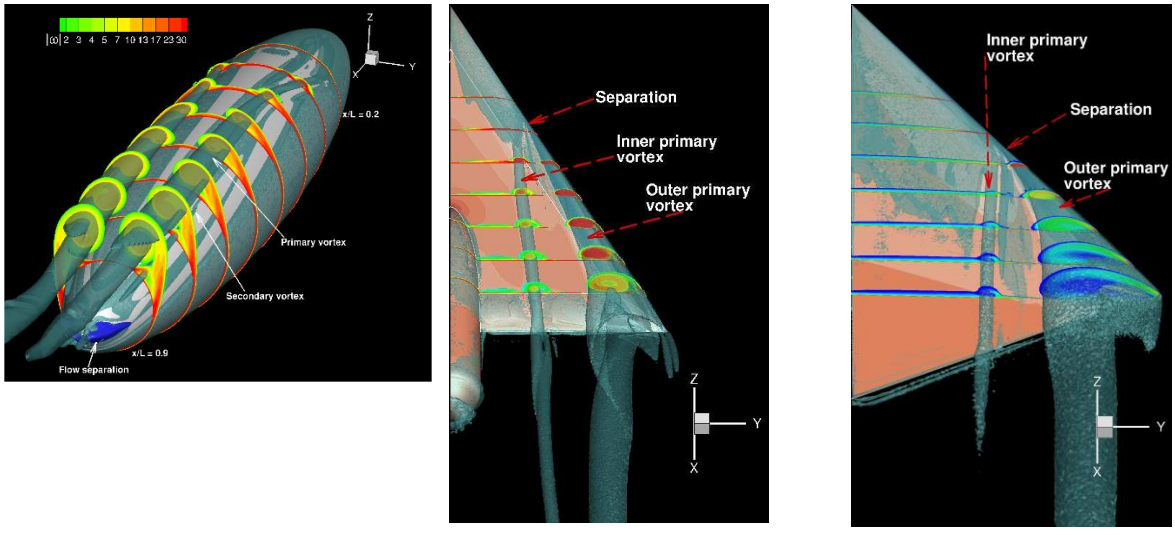

(a) Spheroid (b) Delta wing (c) Diamond wing

Figure 1: Flow topology on different configurations.

The other case investigated is the flow over a diamond wing which is based on the experimental study conducted in the NATO/AVT-183 task group [7] [8]. The geometry is a diamond wing with leading and trailing-edge sweeps of 53° and -26.5°, respectively. In the experiments, the geometry is mounted on a tunnel floor wall with a peniche with standoff distance of $0.075c_r$, where c_r is the root chord which is 1.2m and tests were conducted at a free stream Mach number of 0.15 and Reynolds number based on the mean aerodynamic chord of $2.7x10^6$ and the incidence angle range of 10° to 15° with an increment of 1°. For the present numerical investigation, the incidence angle of α = 12° was chosen as the flow separates midway along the blunt leading edge. Global flow field characteristics associated to the incidence angle of 12° are depicted in *Figure 1*(c) which displays flow separation and the inner and outer primary vortices.

3. Turbulence Modeling

Separated vortex flows investigated in the current study involve separation from a smooth body surface and formation of vortices. Often the vortex interaction with the attached boundary layer exposed to an adverse-pressure gradient leads to secondary vortices where anisotropy of normal Reynolds stresses is observed in experimental investigations [5]. Over the years, extensions to EVMs have been introduced to improve predictions of vortex flow and normal Reynolds stress anisotropy. In the present study EVMs coupled to a rotational correction (RC) approach [9] and the Quadratic Constitutive Relation (QCR) [10] which improve the prediction of the vortex strength and the anisotropy of normal Reynolds stresses are employed. For the present study the Spalart-Allmaras one-equation [11] and the Menter SST k-ω [12] turbulence models are considered. In the present study both models coupled to RC and QCR are employed and in the discussion they are denoted as SA-RC-QCR and SST-RC-QCR.

Concerning RSMs, often the application of differential RSMs to flows involving complex flow phenomena leads to numerical stability problems due to numerical stiffness. This may be one of the reasons for not carrying out investigations with differential RSM in the earlier AVT studies [1]. Recently at DLR, a mathematically exact transformation of the length-scale-providing equation coupled to RSM was studied and demonstrated that such a transformation can significantly improve the stability of RSM for complex industrial flows. In the current study, the SSG/LRR Reynolds stress model [13] developed at DLR within the FLOMANIA project is considered. The ln(ω) length-scale equation [14] coupled to SSG/LRR-RSM, which improves the stability of RSM for complex flows, is employed in the current study and in the discussion the model predictions are denoted RSM.

4. Numerical Methods

In the current investigation the unstructured compressible DLR flow solver TAU is used. Details about the DLR TAU code can be found in [15]. The inviscid fluxes of the main-flow equations are calculated by a central scheme with matrix artificial dissipation. For the turbulence equations, the convective fluxes are approximated with a second-order Roe scheme in the RSM and an Average-of-flux scheme in SA-RC-QCR investigations. The viscous fluxes of the main flow and the diffusion fluxes of the turbulence equations are discretized using central differences.
Steady computations are performed using a semi-implicit lower-upper symmetric Gauss-Seidel (LUSGS) method. For unsteady RSM computations, time-accurate computations are carried out with a 2^{nd}-order dual time-stepping scheme.

5. Performance Evaluation of RSM

Since the objective is to evaluate the predictive capabilities of an RSM model formulation for separated vortex flows, investigations are carried out for the flow over a spheroid, delta wing and diamond wing. All the test cases demonstrate separation from a smooth body surface and subsequent vortex formation. Here, the challenge is the accurate prediction of incipient separation and the strength of the vortices. To evaluate the performance, predictions are compared with available experimental data and EVM predictions.

5.1. Spheroid

The flow over a prolate spheroid at the incidence of $\alpha = 20°$ is investigated. Here, first, grid refinement and grid topology investigations are carried out, and later performance studies are conducted.

5.1.1. Grid refinement study

To keep spatial discretization errors on the predictions as low as possible, a grid refinement study is performed using RSM. For this purpose, two grid types with varying resolution from very coarse to fine are created and employed here. One grid family is a completely hexahedral one and the other is a hybrid grid family consisting of hexahedrons in the near-wall region and tetrahedrons in the remainder of the computational domain. A depiction of the two grid types is shown in Figure *2*. Details of the grid resolution are given in the Table 1.

Table 1 Grid details for the spheroid test case. Number of points in millions.

Grid	**Very coarse**	**coarse**	**Medium**	**Fine**
Hexahedra	0.12	1	7.5	61
hybrid (SOLAR)	-	3.8	11.4	35.5

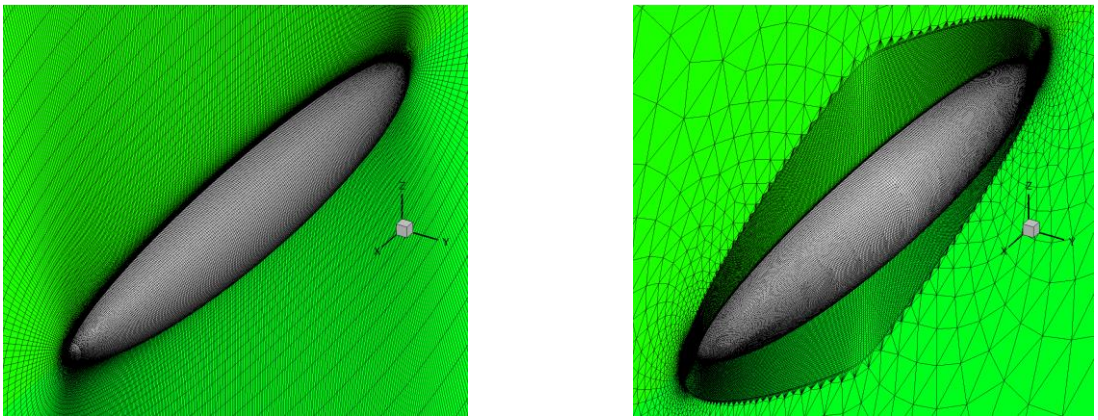

(a) Hexa grid (b) Hybrid grid

Figure 2: Overview of hexahedron and hybrid grids for the spheroid.

The grid convergence of the force coefficients delivered by RSM is shown in Figure *3*. On both grid types convergence of lift and drag with the refinement of the grid is within reach. On the last two fine grids, almost identical force coefficients are obtained on the hexahedra and hybrid grids and the results on the finest grids are almost independent of the grid type.

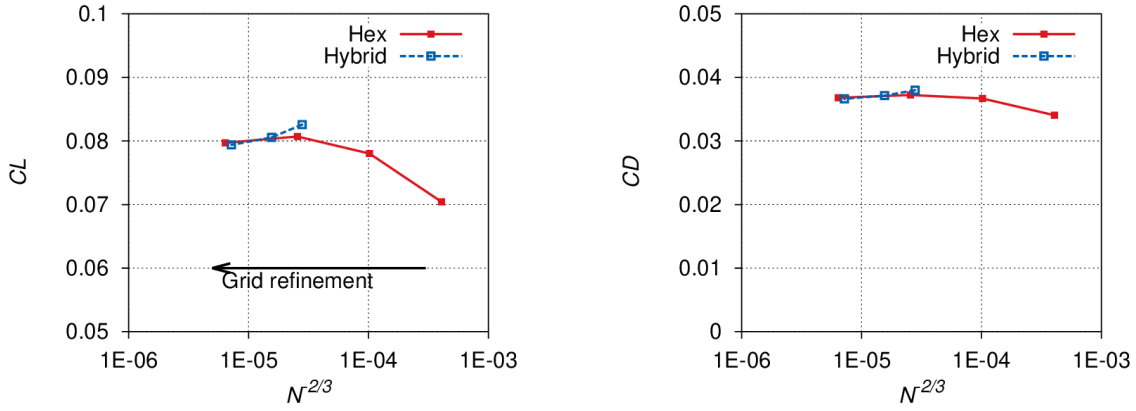

(a) Lift (b) Drag

Figure 3: Grid refinement study on hexahedra and hybrid grids for the spheroid.

A comparison of the pressure coefficient distributions at two different streamwise sections obtained on different hexahedra grid levels is shown in Figure 4. Here, the cp along the azimuthal direction from windward side to leeward side of the spheroid is shown, the direction is shown in Figure 4(b). On all the grids, flow acceleration up to $\varphi = 90°$ is predicted. Beyond this location, flow separation and the subsequent formation of a primary vortex occur. The local cp_{min} in the range $135° < \varphi < 180°$ represents the pressure distribution associated with the primary vortex location. As can be seen, the local cp_{min} is not predicted on the very coarse grid due to the weak vortex in the simulation. However, as the grid is refined the vortex strength increases and the local cp_{min} exhibits stronger peaks. On the medium and fine grids almost identical cp_{min} is predicted and overall the cp on both medium and fine grids does not change significantly with grid refinement.

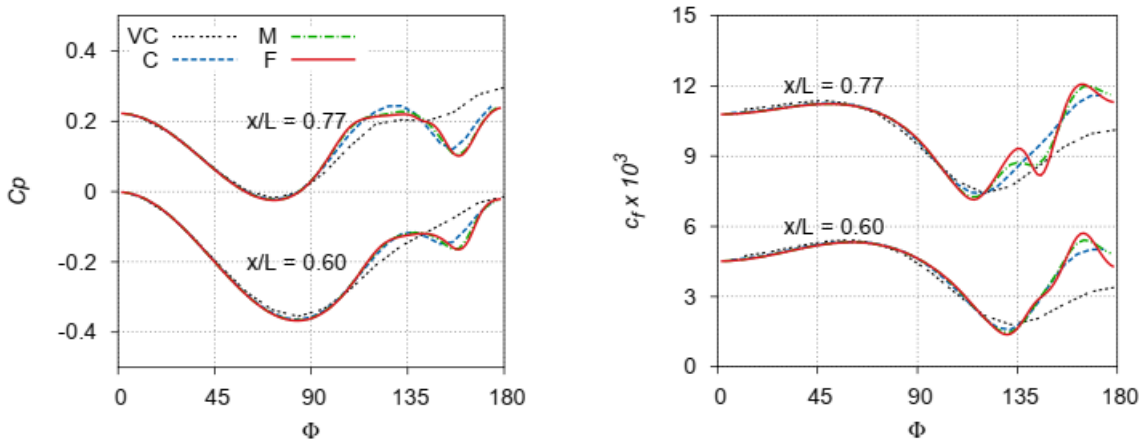

(a) cp (b) cf

Figure 4: Grid refinement on hexahedra grid for the spheroid. VC: very coarse, C: coarse, M: medium and F: fine.

In Figure 4(b) the cf distribution at two different streamwise sections is shown. Local cf_{min} and cp_{max} represent flow separation and reattachment, respectively. At x/L = 0.6, flow separation is predicted almost at the same location on all grids. However, reattachment is not clear on the very coarse grid due to the weakness of the vortex. On the other grids, reattachment is predicted almost at the same location. At x/L = 0.77, primary separation and reattachment are predicted at the same locations on the coarse to fine grids. Minor differences are observed in the location of secondary separation and reattachment. On the very coarse and coarse grids, the secondary separation is not predicted and, thus, local cf_{min} and cf_{max} are not observed in the region $110° < \varphi < 150°$. On the medium and fine grids, the secondary flow separation and reattachment are predicted at the same locations. However, differences are observed in the local cf_{max} which is due to the stronger secondary vortex observed on the fine grid. Overall, the qualitative and quantitative similarity in the results of cp, cf, lift and drag on the medium and fine hexahedra grids indicate that grid converged results are within reach.

In Figure 5, cp and cf obtained on the fine hexahedra and hybrid grids are compared. On both grids almost identical pressure and very close skin-friction distributions are predicted by the RSM. A comparison of the contours of the vorticity magnitude and the turbulent kinetic energy (both not shown here) unveiled again almost identical distributions. Overall, the RSM delivered almost identical or matching results on the fine grids independent of the grid topology. For the further studies, only the fine hexahedra grid is employed.

5.1.2. Turbulence model study

To evaluate the performance of turbulence models, investigations are carried out with the SA-RC-QCR, SST-RC-QCR and RSM turbulence models and the predictions are compared to the available experimental data [5].

In Figure 6 (a), the surface pressure distribution along the azimuthal direction at streamwise locations of x/L = 0.6 and 0.77 are shown. In the experiments the local cp_{min} in the region of 135°

< φ < 180° indicates the location of the primary vortex. In all the predictions the primary vortex location is observed slightly inboard compared to the experiments. The pressure associated with the primary vortex is underpredicted with all the turbulence models applied. A possible reason for this discrepancy is the weaker vortex compared to the experiments.

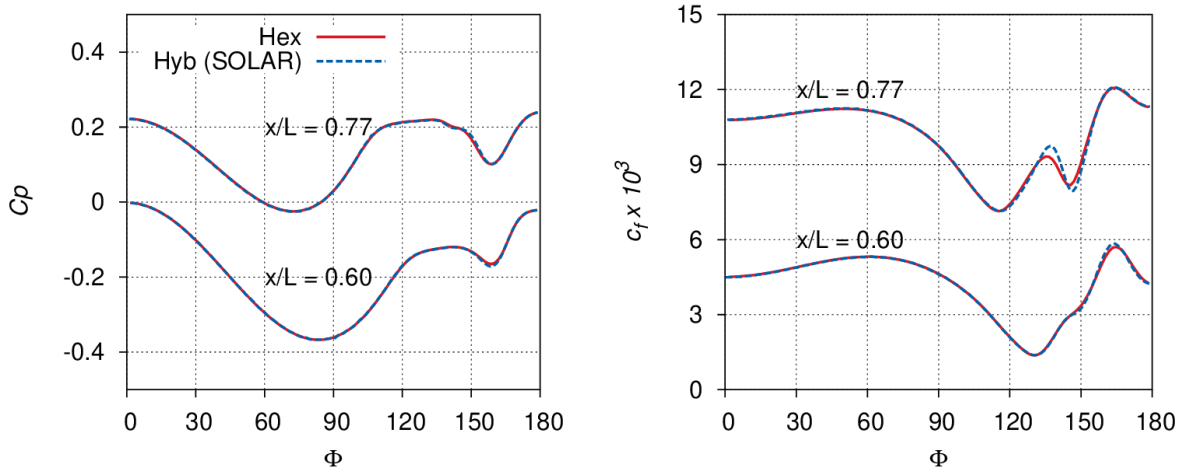

(a) cp (b) cf

Figure 5: Grid topology study on hexahedra and hybrid grids for spheroid.

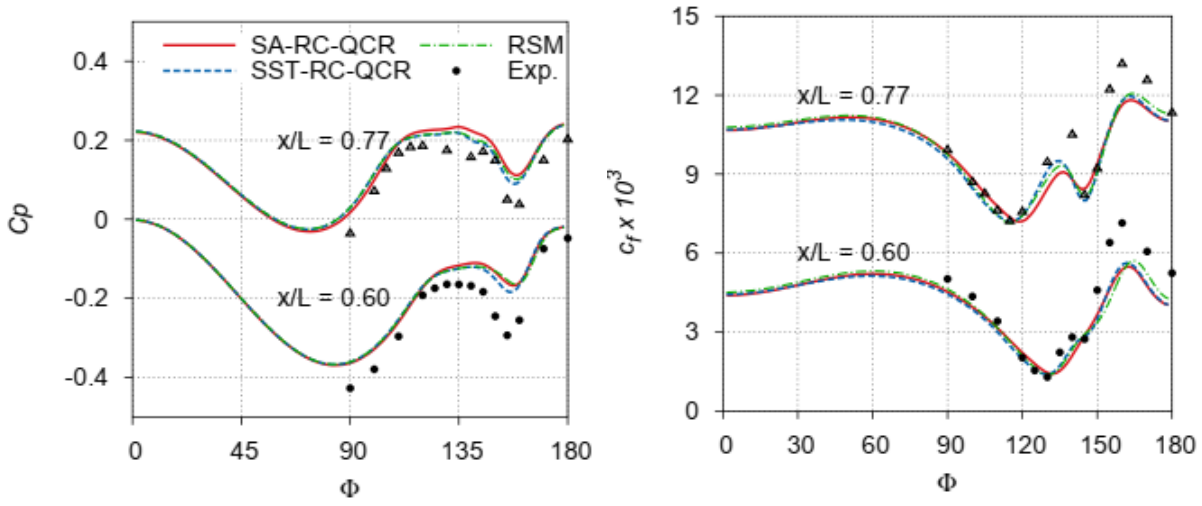

(a)cp (b)cf

Figure 6: Turbulence model study for the spheroid on the hexahedra fine grid.

The pressure plateau in the experiments in the region of 112° < φ < 145° at x/L = 0.6 and 100° < φ < 135° at x/L = 0.77 unveils the extent of separated flow. All the models deliver almost similar pressure levels in the separated region and the results exhibit a satisfactory agreement with the experiments.

In Figure 6(b), cf along the surface in the azimuthal direction at two different streamwise locations is shown. In the experiments local cf_{min} and cf_{max} indicate local flow separation and reattachment, respectively. At x/L = 0.6 all the models reproduce the experimental separation location. At x/L = 0.7, local cf_{min} is observed at two locations in the experiments. At $\varphi = 120°$ the local cf_{min} represents the primary separation and at $\varphi = 140°$ local cf_{min} unveils a secondary separation. In the case of SA-RC-QCR the primary separation is slightly delayed whereas the RSM and SST-RC-QCR deliver the experimental separation point. Concerning the secondary separation, all the models reproduced the experimental secondary separation point. The cf_{max} denotes the region close to flow reattachment. In the region $150° < \varphi < 180°$, compared to the experiments, the reattachment is predicted inboard with all the turbulence models. Again, the cf_{min} level is underpredicted which is linked to the vortex strength that is underpredicted.
Contours of the vorticity magnitude delivered by different turbulent models at x/L= 0.77 is shown in Figure 7. As can be seen, all the applied turbulence models predict almost the same level of vorticity magnitude in the separated shear layer and in the secondary vortex region. In the core of the primary vortex, minor differences can be observed. In the RSM and SST-RC-QCR slightly higher vorticity magnitude values are predicted compared to the SA-RC-QCR. This marginally lower vorticity magnitude in the SA-RC-QCR predictions lead to marginally higher pressure on the surface in the region of the primary vortex, see Figure 7(a).

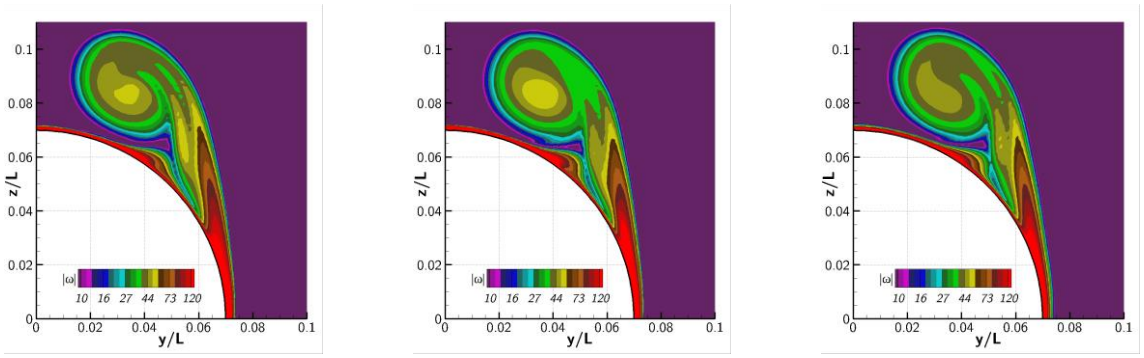

(a) RSM (b) SST-RC-QCR (c) SA-RC-QCR

Figure 7: Contours of vorticity magnitude on the spheroid at x/L = 0.7.

In Figure 8, contours of turbulent kinetic energy (TKE) are shown. In the separated shear layer the predicted values show a still acceptable agreement with the experiment, although one can doubt the quality and reliability of the measured data and, thus, a more profound assessment is not possible. In the region where the shear layer from the secondary separation interacts with the free shear layer emanating from the primary separation, very high TKE is observed in the experiments. This trend is reproduced in SST-RC-QCR and RSM and the predicted value levels agree well with the experimental data.

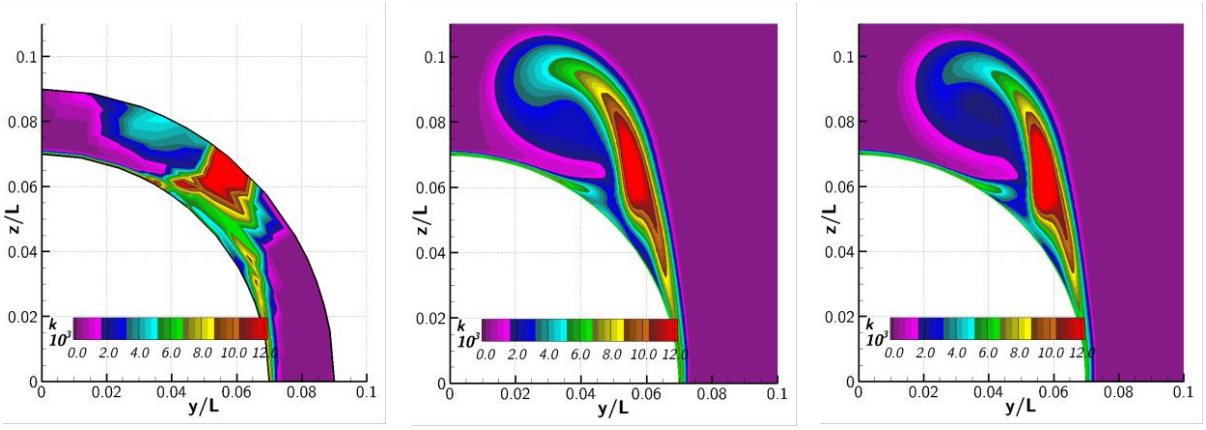

(a) Exp. (b) RSM (c) SST-RC-QCR

Figure 8: Contours of turbulence kinetic energy on the spheroid at x/L = 0.7722.

To visualize the resolved vortices, the iso-surface of the vortex criterion λ_2 is shown in Figure 9. As can be seen all the applied models resolve both primary and secondary vortices well. To unveil the separated region, the iso-surface of the streamwise velocity is also shown with blue color in the same figure. From the figure it is evident that all the models predict almost the same size of separation at the base of the spheroid.

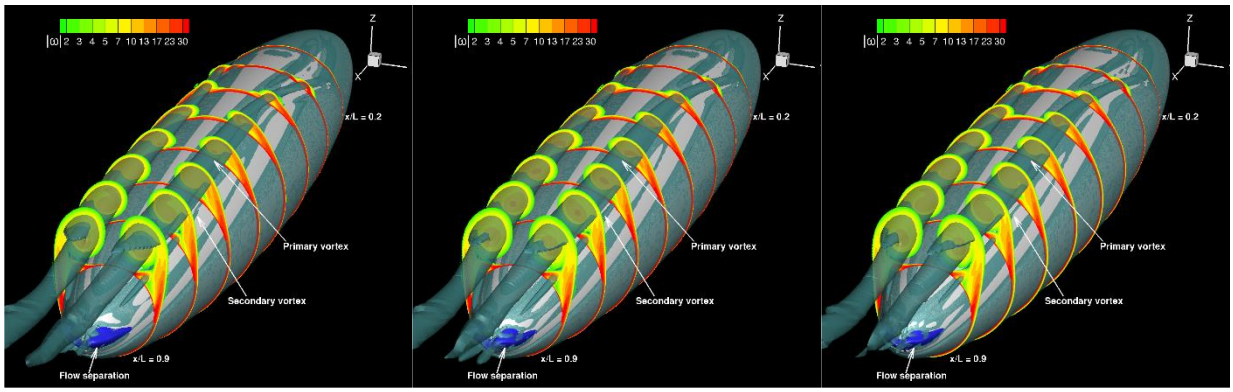

(a) RSM (b) SST-RC-QCR (c) SA-RC-QCR

Figure 9: Iso-surface of λ_2 = -1 and streamwise velocity u = 0 for the spheroid.

Overall, all the applied models deliver almost similar predictions and the results are observed to be in good agreement with the experimental data. EVMs when coupled with RC and QCR tend to deliver predictions of very similar qualitative and quantitative levels as a full differential RSM for the current test case. Differences in cp and cf in the primary and secondary vortex regions may be emanating from the differences in vortex strength. In the current investigation, grid refinement studies showed that not much improvement can be observed by further grid refinement. It may be that further improvement of physical modeling is required to improve vortex strength.

5.2. Deltawing

The second test case considered is the flow over a swept delta wing with round leading edge. For this test case, first, a grid refinement study is carried out and later a turbulence model study is conducted to evaluate the turbulence model performance. Finally, the effect of the free stream Reynolds number is investigated for the same geometry.

For the present study, the Centaur grid generation tool was used to generate grids. Three grids successively refined both in boundary-layer and far-field regions were generated. The coarse grid has 6 million points while the medium and fine grids have 15 and 44 million points, respectively. To study the grid topology effect, another grid with hexahedra cells in the near-wall region and tetrahedra cells in the far-field is generated using the SOLAR grid generation tool.

5.2.1. Grid refinement study

A grid refinement study is carried out using the RSM. The effect of grid resolution on the predicted flow topology is assessed based on the surface pressure distribution. In Figure 10, the contours of the pressure coefficient distribution on the surface along with surface skin-friction lines are shown. On all grid levels flow separation from the leading-edge occurs at x = 0.4 which is denoted by the region of low cp moving from the round leading-edge to the inboard section of the wing. On all grids, the inner primary and outer primary vortices are resolved. On the coarse grid a second outer primary vortex is predicted on the coarse grid which can be seen at x = 0.7. However, on the finer grids this trend is not observed.

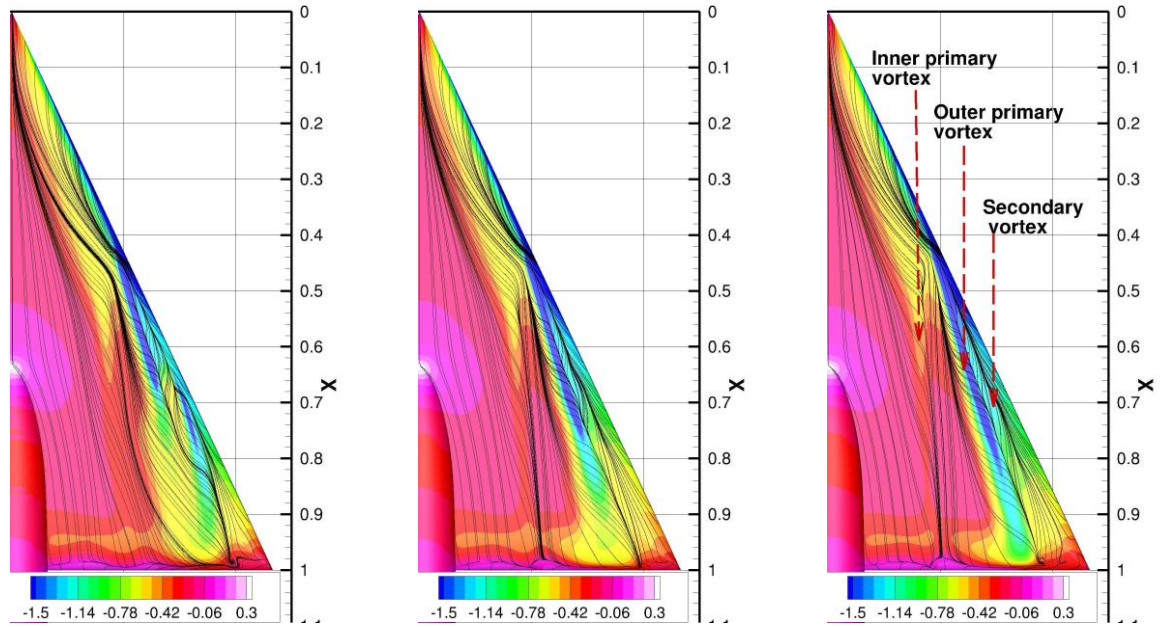

(a) Coarse (b) Medium (c) Fine

Figure 10: Surface pressure distribution and skin-friction lines on the delta wing for different grid levels

Further differences can be seen in the pressure distribution associated with the vortices on different grid levels. The region with low pressure associated with the outer primary vortex is extended in streamwise direction with the grid refinement. The reason for this trend is the vortex strength which increases as the grid is refined. On the medium and fine grids, almost similar pressure distributions are predicted in the inner primary vortex region.

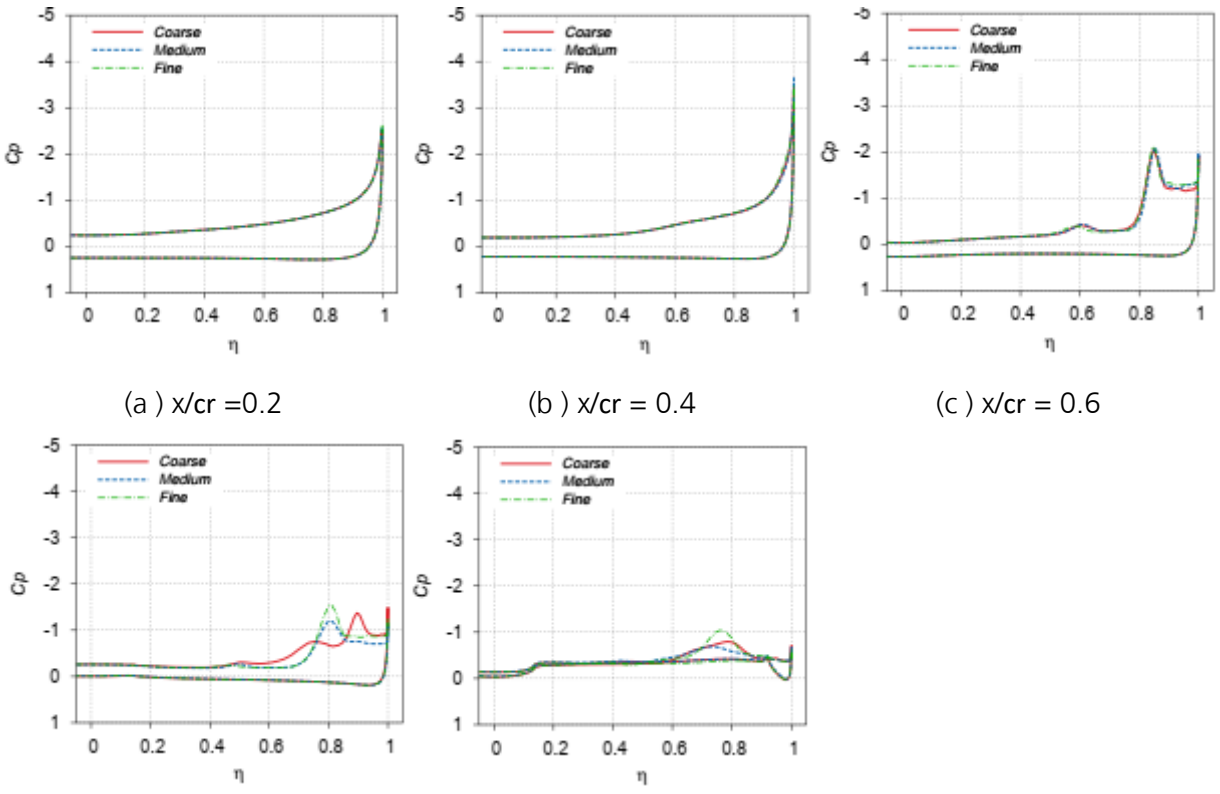

(a) x/cr =0.2 (b) x/cr = 0.4 (c) x/cr = 0.6

(d) x/cr = 0.8 (e) x/cr = 0.95

Figure 11: Pressure coefficient distribution for the delta wing on different grid levels.

For a quantitative comparison, cp at different streamwise sections obtained on different grid levels is shown in Figure 11. Due to attached flow in the region upstream x/cr = 0.4, almost identical pressure distributions are obtained on all grids. At x/cr = 0.6, the suction peak at the spanwise location of η = 0.85 indicates the low pressure associated with the outer primary vortex core which is delivered almost identical on all the grids. Another local cp peak at the spanwise location of η = 0.6 renders the suction pressure associated with the inner primary vortex which is also almost identical on all the grids. However, at x/cr = 0.8 differences in the suction pressure can be observed. On the coarse grid, the cp peak moves outboard which is due to a second primary vortex which is generated due to flow separation from the leading-edge. On the medium and fine grids, the outer primary vortex is located at the spanwise location of η = 0.8 and the suction peak associated with

the vortex increases with the grid refinement due to stronger vortex on the finest grid. At $\eta = 0.9$, a higher suction peak on the finest grid is delivered.
Overall, on the medium and fine grids, almost the same pressure distribution for the inner primary vortex is observed. Concerning the outer primary vortex, the location of the outer primary vortex is observed at the same location on the medium and fine grids. For the further investigations the finest grid employed here is considered.

5.2.2. Grid topology investigations

An additional grid generated using the SOLAR grid generation tool is employed to carry out grid topology investigations. On the SOLAR grid the surface is mainly resolved with quadrilateral cells and, as a result, the boundary-layer regions are resolved with hexahedra cells and the remaining region is filled with tetrahedra cells. The major difference between the Centaur hybrid and SOLAR hybrid grids is the near-wall grid topology. Here the main objective is to evaluate the influence of the near-wall cell types on the separated vortical flow. For this purpose, the SOLAR grid resolution is kept as close to the Centaur fine grid resolution as possible. The finest Centaur grid has a total number of points of 44 million while the SOLAR grid has 42 million grid points.
Surface pressure distributions and skin-friction lines obtained on the Centaur and SOLAR grids are shown in Figure 12. On both grids flow separation from the round leading edge is predicted almost at the same location $x = 0.4$ and resolved inner and outer primary vortices are present. Minor differences in the suction pressure associated with the vortices can be seen. On the SOLAR grid, the suction pressure is slightly lower compared to the Centaur grid. This is due to the marginally coarser far-field grid resolution leading to a weaker vortex strength compared to the Centaur grid. To demonstrate the minor differences in cp, sectional pressure distribution at $x/cr = 0.6$, 0.8 and 0.95 are shown in Figure 13. As can be seen in the figure, the suction peak associated with the outer primary vortex is slightly lower on the SOLAR grid compared to the Centaur grid.
Based on the grids used in the current study, no great influence of the grid topology on the predictions is observed. For the further studies, the hybrid Centaur fine grid is used because it predicted a higher suction peak compared to SOLAR fine grid.

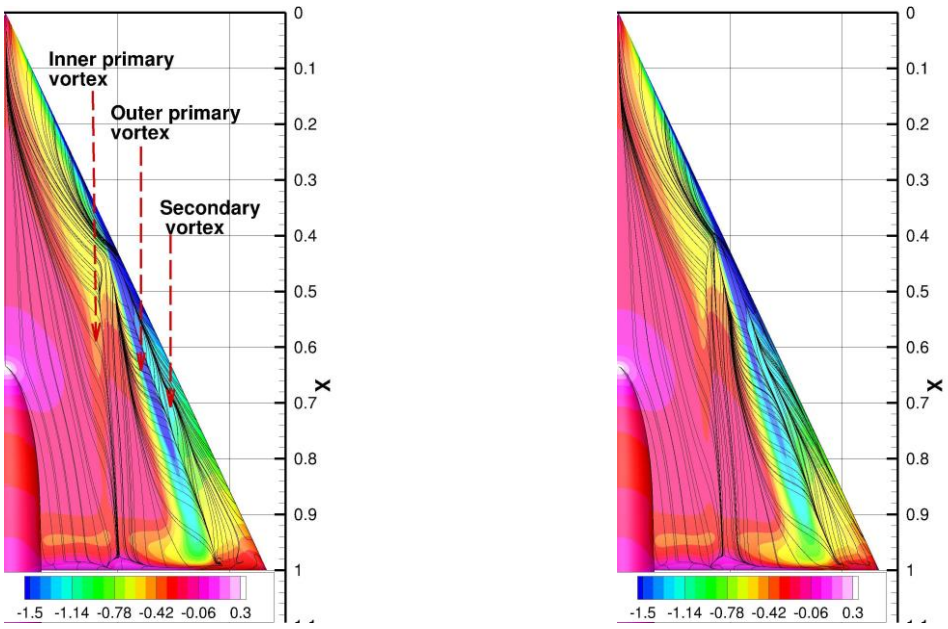

(a) Centaur (b) SOLAR

Figure 12: Pressure and coefficient and skin-friction lines on the delta wing on the fine.

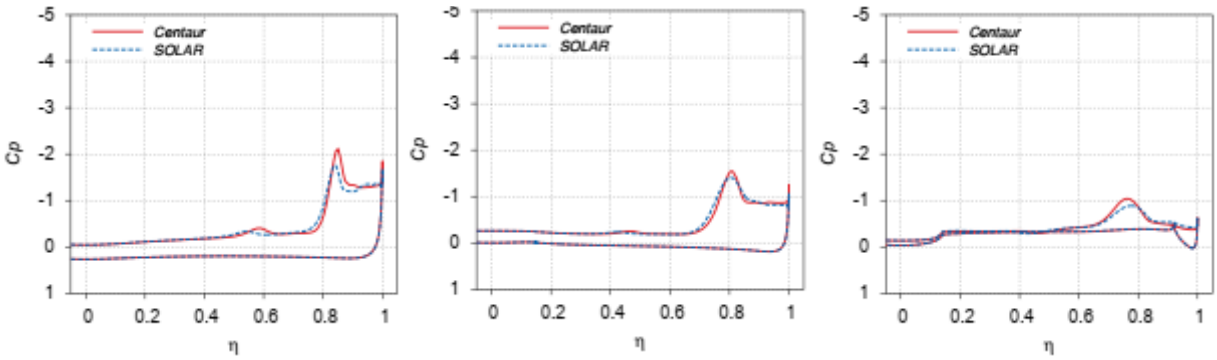

(a) $x/c_r = 0.6$ (b) $x/c_r = 0.8$ (c) $x/c_r = 0.95$

Figure 13: Influence of grid topology on pressure coefficient distribution for the delta wing.

5.2.3. Turbulence model study

To evaluate the turbulence model capabilities, investigations are carried out with the SA-RC-QCR and RSM on the fine Centaur grid. To unveil the resolved vortices, the iso-surface of λ_2 along with the vorticity contours at several streamwise locations are shown in Figure 14. Both the SA-RC-QCR and RSM resolve inner and outer primary vortices. From the contours of the vorticity magnitude in the inner primary vortex, it is evident that the resolved vortex is weaker compared the one delivered

by RSM. The vorticity contours in the outer primary vortex unveil that both SA-RC-QCR and RSM predict almost the same vorticity magnitude up to x/cr = 0.8. However, downstream of this location in the SA-RC-QCR predictions a low vorticity magnitude in the vortex is predicted. To display the effect of the vorticity magnitude on the pressure distribution, the contours of cp along with the skin-friction lines are shown in Figure 15. From the skin-friction lines it is evident that the SA-RC-QCR and RSM resolve both the inner and outer primary and secondary vortices. Downstream of x/cr = 0.8, in the SA-RC-QCR the pressure associated with the outer primary vortex is higher compared to the RSM. This is due to weaker vortex predicted in the SA-RC-QCR as discussed earlier.

To evaluate the performance of the applied turbulence models, sectional cp distributions delivered by the RSM and SA-RC-QCR are compared to the experimental data in Figure 16. At x/cr = 0.2, both models predict attached flow and deliver almost identical pressure distribution and agree well with the experiments. At x/cr = 0.4, the flow is still attached in the experiments. This trend is reproduced in the RSM predictions. However, in the case of SA-RC-QCR, the flow separation occurs upstream of this location and subsequent vortex formation begins. As a result, low pressure in the vortex core is exerted on the surface which is rendered in the cp spike at η = 0.9. This shows that in the SA-RC-QCR predictions flow separation occurs earlier than in the experiments which lead to a mismatch of cp with the experimental data at this location.

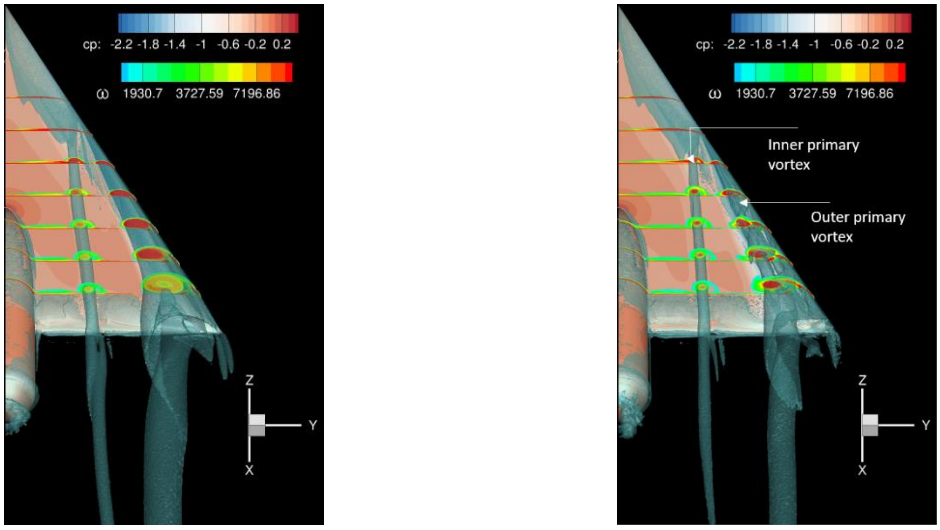

(a) SA-RC-QCR (b) RSM

Figure 14: Iso-surface of λ_2 and the contours of vorticity magnitude delivered by SA-RC-QCR and RSM for the delta wing.

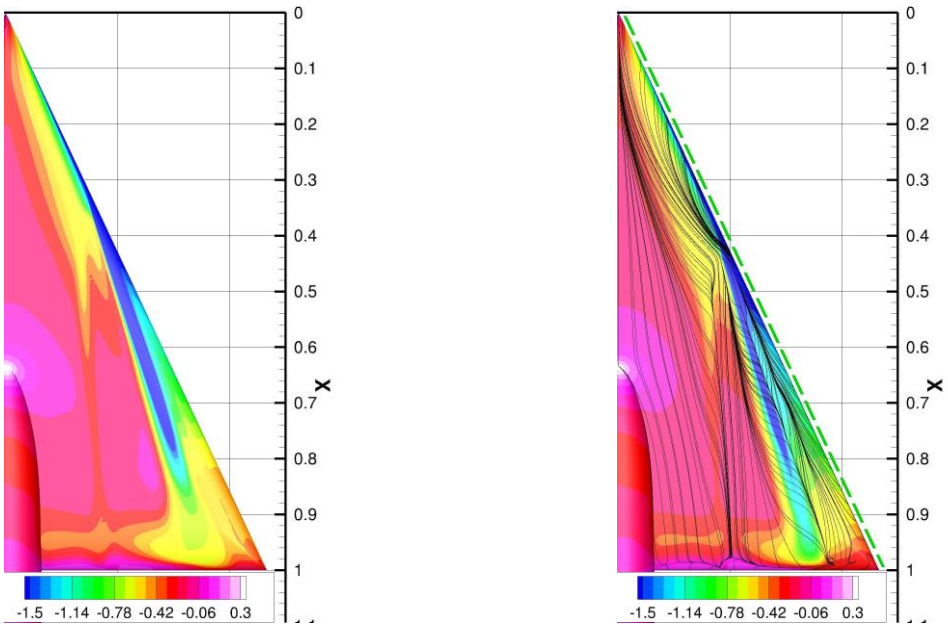

(a) SA-RC-QCR (b) RSM

Figure 15: Pressure coefficient and skin-friction lines on the fine Centaur grid; turbulence model study for the delta wing.

At x/cr = 0.6 and 0.8, the suction peaks in the experimental pressure distribution indicate the location and associated pressure distribution of the inner primary and outer primary vortices. Low pressure associated with the outer primary vortex is predicted well with the SA-RC-QCR and RSM, however, the vortex is located too far inboard in the predictions. In the outboard separated region, $\eta > 0.9$, SA-RC-QCR delivers higher pressure compared to the experiments. The pressure distribution delivered by the RSM yields a clearly better agreement with the experimental cp. In the experiments, the inner primary vortex location and the associated pressure is rendered with the local cp_{min}. In the SA-RC-QCR and RSM predictions, the pressure associated with the primary vortex is underpredicted. Concerning the location, the SA-RC-QCR predicts the vortex too far inboard while RSM delivers the location which is in between experiments and SA-RC-QCR predictions and, thus, closer to the experiments. At x/r = 0.95, in the SA-RC-QCR predictions an almost flat cp-distribution is delivered due to the weaker outer primary vortex whereas in the case of RSM cp associated with the outer primary vortex is reproduced as in the experiments.

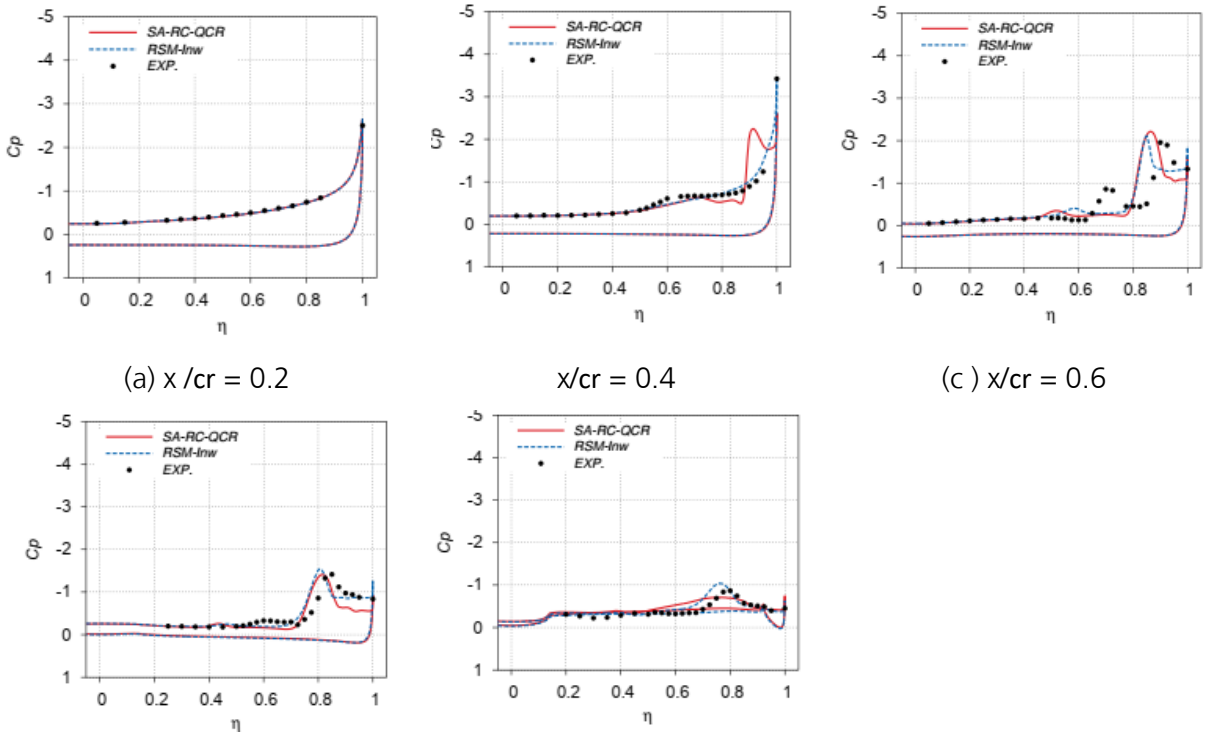

(a) x /cr = 0.2 x/cr = 0.4 (c) x/cr = 0.6

(d) x/cr = 0.8 (e) x/cr = 0.95

Figure 16: Pressure coefficient distribution delivered by SA-RC-QCR and RSM on the fine grid.

Overall, the RSM-based predictions are observed to be in better agreement with the experiments with respect to the separation location from the leading edge, pressure associated with the primary vortex and the separated region on the outboard section of the wing. However, still the remaining challenge is to accurately predict the inner primary vortex location and the pressure distribution associated with the vortex.

Since the RSM delivered better predictions compared to SA-RC-QCR, the further studies are carried out with the RSM.

5.2.4. Reynolds number study

To study the influence of the Reynolds number on the incipient separation and subsequent vortex formation, investigations are carried out at a freestream Mach number of 0.4 and a Reynolds number of 2 million, 3 million and 6 million at the incidence angle α = 13.3°. For this investigation, the finest Centaur grid used in the earlier studies is employed.

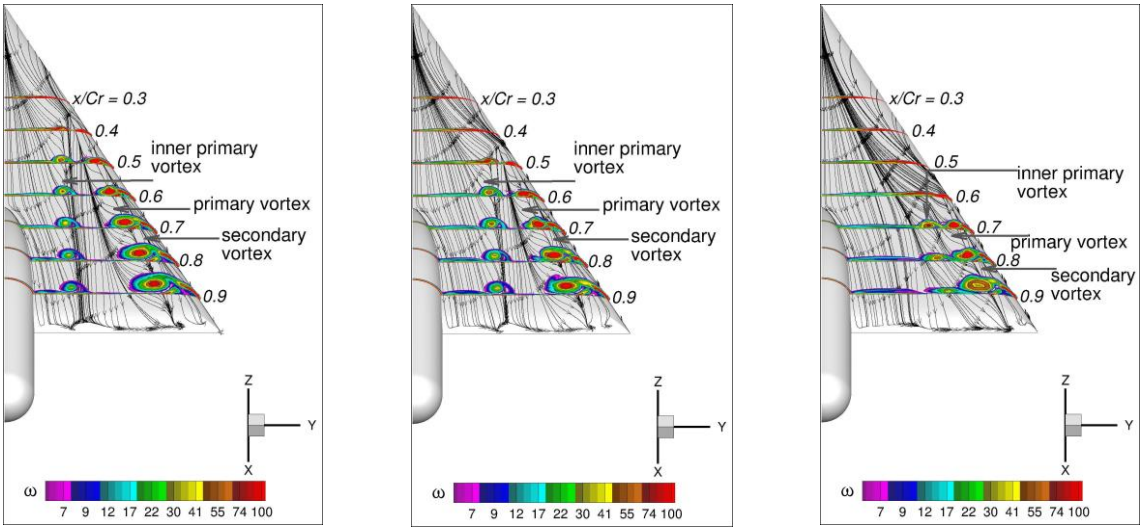

(a) Re = 2 million (b) Re = 3 million (c) Re = 6 million

Figure 17: Reynolds number study; Contours of vorticity and skin-friction lines.

To display the flow topology obtained at the different Reynolds numbers, skin-friction lines along with vorticity contours at different streamwise sections are shown in Figure 17. From the figure it is evident that the separation from the round leading edge and the formation of the inner and outer primary vortices move downstream with the Reynolds number. To illustrate the downstream movement of the flow separation, cp along the leading-edge of the delta wing at the different Reynolds numbers is shown. The line along which cp is extracted is shown in Figure 18(a) and the extracted cp-distributions are shown in Figure 18(b). At Re = 2 million, the decrease in cp shows attached flow extending up to the chordwise position of x/cr = 0.3. Beyond this location the suction pressure collapses due to flow separation, according to [12]. With increasing Reynolds number the location where the suction pressure collapses moves downstream. This trend indicates downstream movement of flow separation and subsequent vortex formation.

The pressure coefficient distribution along the wing span at several streamwise locations is shown in Figure 19. In the figure, for visualization purpose, the cp distributions obtained at the Reynolds number of 3 million and 6 million are shifted by -2 and -4, respectively. At x/c_r = 0.2 in the experiments, attached flow can be observed with a suction peak located at the leading-edge for all the cases. This trend is reproduced in the numerical predictions. Further downstream of this location, at x/cr = 0.4, still attached flow is evident for the higher Reynolds number cases in the experiments. However, for the Re = 2 million case, higher pressure at the leading-edge is observed due to separated flow. Local suction peaks (cp_{min}) at the spanwise location of η = 0.5 and 0.8 indicate the pressure associated with the outer primary and inner primary vortex cores. The outer primary vortex position and the associated pressure level, shown with a black arrow in Figure 19(b), are well reproduced in the numerical study. However, the inner primary vortex pressure, shown with a red arrow, is underestimated

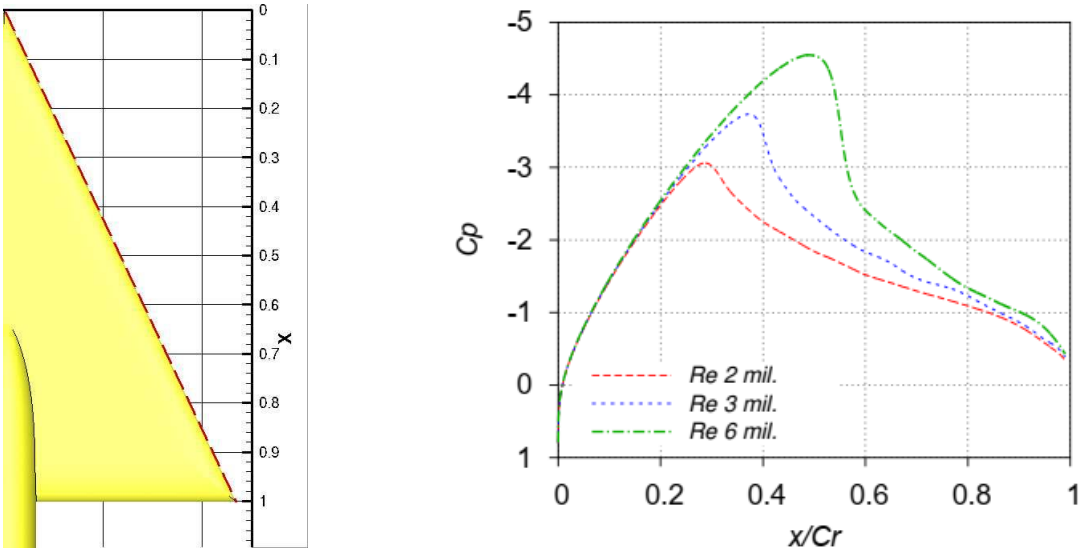

(a) Extracted cp line (b) Cp at leading-edge

Figure 18: Pressure distribution along the leading edge of the delta wing at different Reynolds number.

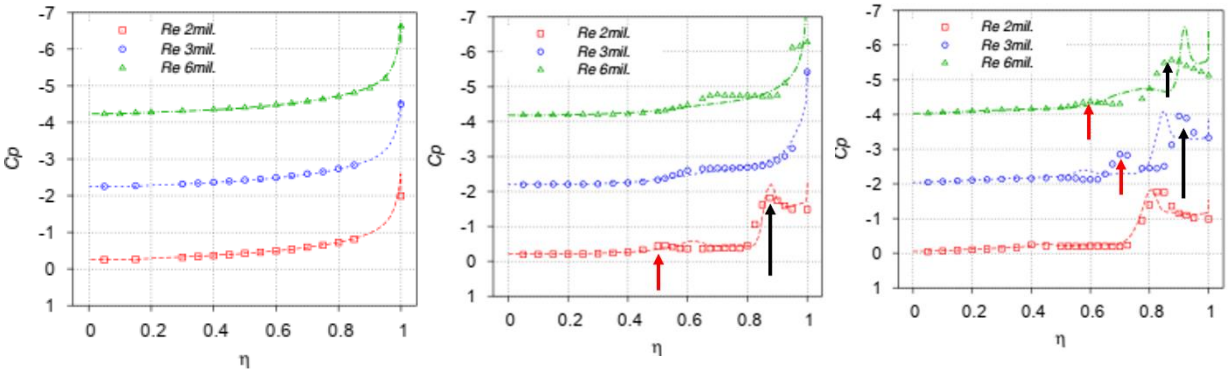

(a) x /cr = 0.2 (b) x/cr = 0.4 (c) x/cr = 0.6

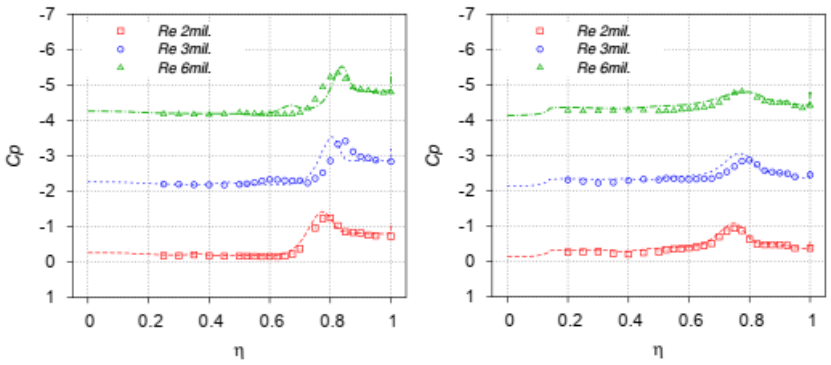

(d) x/cr = 0.8 (e) x/cr = 0.95

Figure 19 Pressure distribution on the suction side of the delta wing for different Reynolds number at $\alpha = 13.3^{\circ}$. Cp offset for successive Reynolds number case is 2.

At x/cr = 0.6, in the experimental pressure distribution, a shift in the location of the suction pressure from the leading edge to the inboard section of the wing and local cp peaks unveil separated flow on the leading edge and inner and outer primary vortices (shown with arrows in Figure 19(c). In the numerical investigations the same trend is observed. However, the location and the associated pressure distribution are underpredicted for the Re of 3 million and 6 million cases. Further downstream, at x/cr = 0.8 and 0.95, an inboard movement of the outer primary vortex and lower cp peaks associated with the inner and outer primary vortices are evident from the experimental data. In the numerical investigation this trend and the pressure levels associated with the outer primary vortex are well reproduced.
Overall, for the case with Re of 2 million, the predictions agree well with the experimental data. For higher Reynolds number cases, major differences are observed at the streamwise station of 0.6. This can be due to an upstream position of the separation point delivered in the investigations compared to the experiments. At the other positions the predictions are in good agreement with the experimental data.

5.3. Diamond wing

The flow over a diamond wing at the incidence angle of 12° is investigated. Here, the objective is to assess how accurate a turbulence model can predict the incipient separation location and the pressure associated with the vortices which are formed as a result of flow separation.

5.3.1. Grid Refinement study

In the current work, the grid generation using the Centaur grid tool is not successful because of problems on the leading edge at the wing tip and as a result only the SOLAR grid generation tool is used. Here, three grids successively refined are generated. The grids have hexahedra cells in the near-wall region and tetrahedra cells in the remainder of the computational domain. The coarse grid has about 10 million grid nodes, while the medium and fine grids have 26 and 43 million nodes. An overview of the grid on the surface and in the farfield is shown in Figure 20(b). The grid refinement study is carried out on the three grid levels discussed earlier. Here the behavior of the results is assessed based on the variation of flow topology and the surface pressure distribution. With the RSM, a steady computation resulted in oscillatory force coefficients. As a result, time-accurate computations are carried out until the force coefficients converge.
Surface skin-friction lines along with the cp contours obtained on different grid levels are shown in Figure 21. On all grid levels, the foot prints of resolved vortex render the inner and outer primary vortices. On the medium and fine grids, a secondary vortex is also resolved whereas on the coarse grid it is not observed. Overall, on the medium and fine grids the flow topology looks almost the same. To display the flow separation from the blunt leading edge, cp along the leading edge is shown in Figure 22(a). The collapse of the suction peak renders the flow separation from leading edge. As can be seen, with the grid refinement the separation point moves upstream along the

leading-edge. On the medium and fine grids only a slight change in the separation location with the grid refinement is observed.

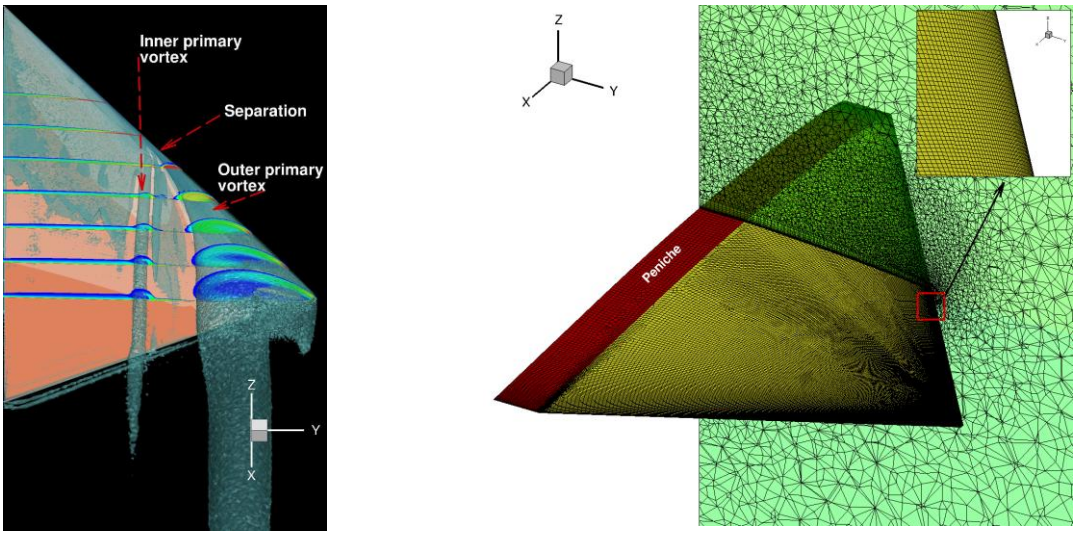

(a) Flow topology (b) Grid (coarse)

Figure 20: Flow topology on the diamond wing at $\alpha = 12^\circ$ and the computational grid on the surface and in the field.

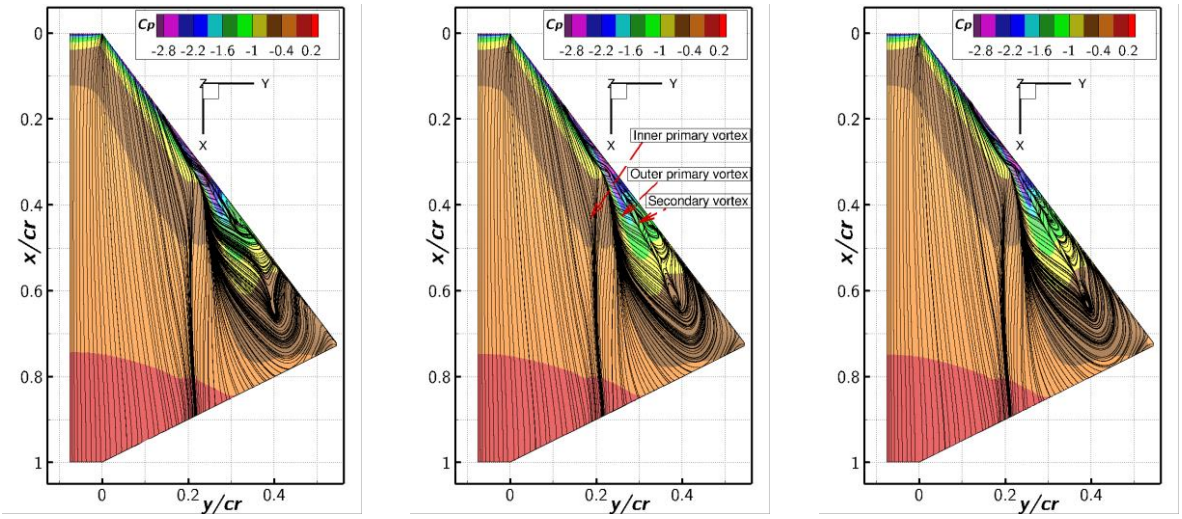

(a) Coarse (b) Medium (c) Fine

Figure 21: Contours of pressure coefficient delivered by RSM on different grids.

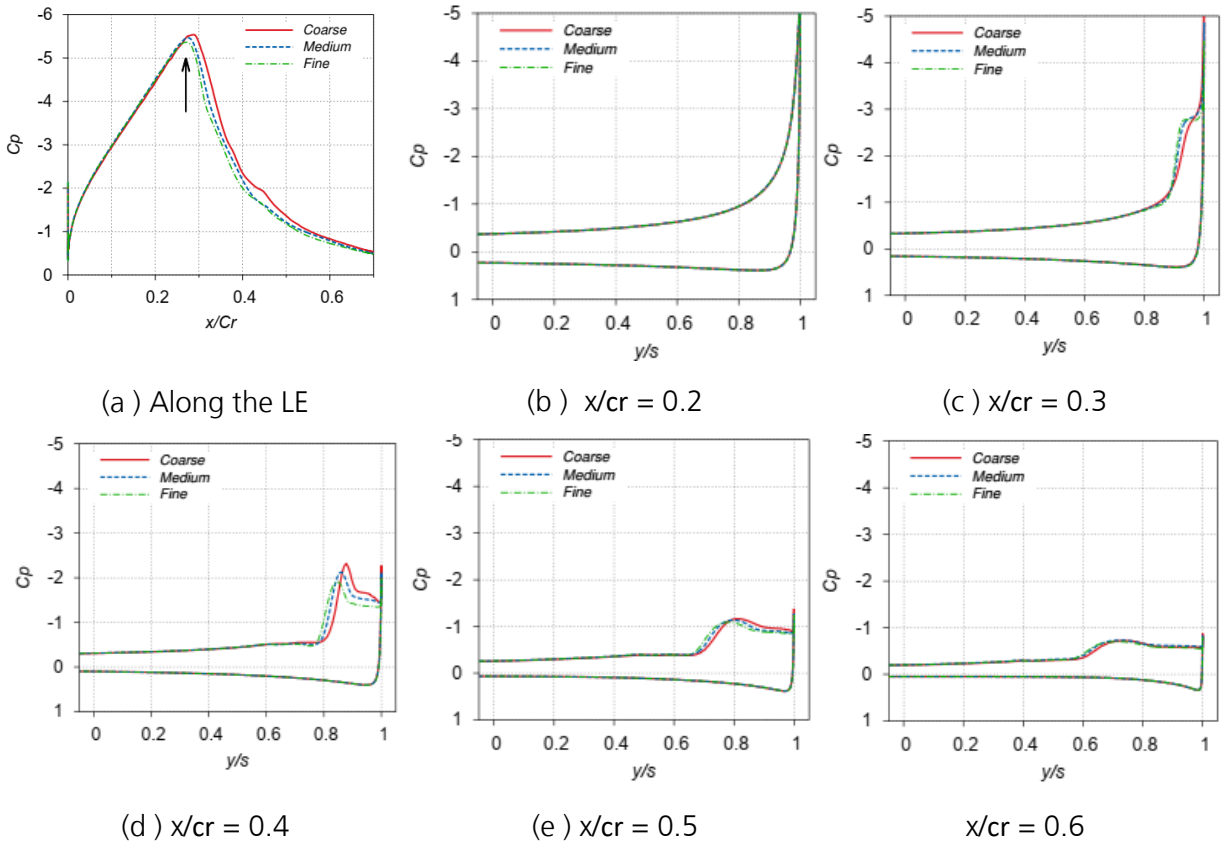

(a) Along the LE (b) x/cr = 0.2 (c) x/cr = 0.3

(d) x/cr = 0.4 (e) x/cr = 0.5 x/cr = 0.6

Figure 22: Cp distribution delivered by RSM at different streamwise sections.

Sectional cp distributions obtained on the different grid levels are shown in Figure 22. At x/cr = 0.1 and 0.2, due to attached flow almost identical pressure distributions are predicted on all grid levels. At x/c r = 0.3, on the medium and fine grids almost identical pressure is delivered. At x/cr = 0.4, with increasing grid resolution higher pressure is predicted in the separated zone, y/s > 0.9. At x/c r = 0.5 and 0.6 almost identical pressure is delivered on the medium and fine grids. Overall, the grid refinement study unveils that the predictions do not change much on the medium and fine grids. For the further investigations, the fine grid is employed.

5.3.2. Turbulence model study

In this study, investigations are carried out with the SA-RC-QCR and RSM on the fine grid discussed in the previous chapter. The SA-RC-QCR computation converged in steady computation mode, whereas with the RSM time-accurate computations are required to flatten out the oscillations in the force coefficients observed in a steady computation. In Figure 23, the iso-surface of λ_2 and vorticity contours at several streamwise sections are shown. From the figure it is apparent that the SA-RC-QCR and RSM deliver both the inner and outer primary vortices. In the case of the SA-RC-QCR separation from the leading-edge occurs between the streamwise stations of 0.2 and 0.3 whereas in the cases of RSM, it occurs at x/c r = 0.3. Vorticity contours at x/c r = 0.6 display reduced

levels of the vorticity magnitude in the SA-RC-QCR and RSM results compared to the upstream stations. The trend of reduced levels of vorticity magnitude is also observed in the experiments [8]. In the case of RSM the level of vorticity magnitude in the core is lower than in the SA-RC-QCR predictions. Low vorticity in the vortex core indicates the possibility of vortex breakdown.

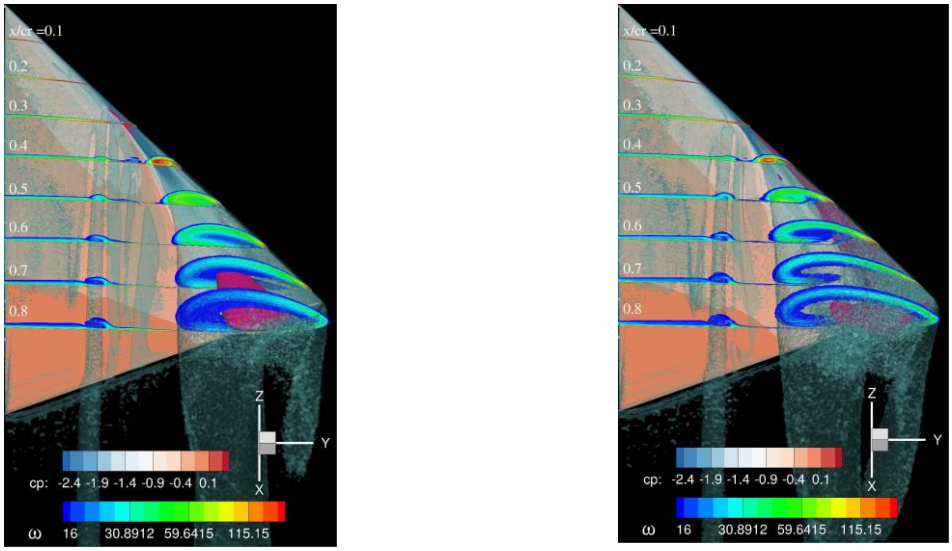

(a) SA-RC-QCR (b) RSM

Figure 23: Iso-surface of λ_2 and the contours of vorticity magnitude on fine grids.

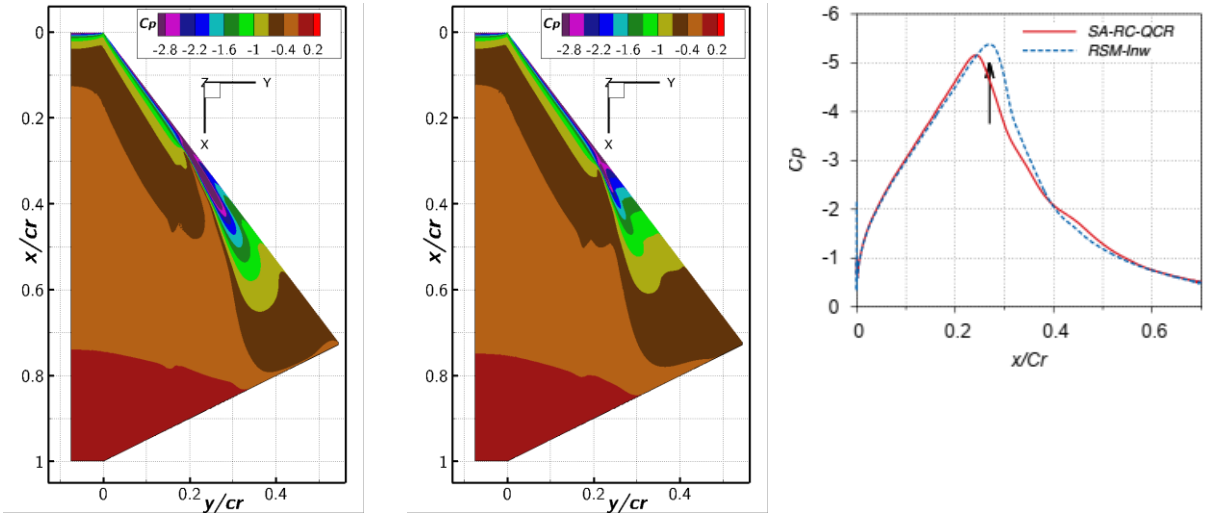

(a) SA-RC-QCR (b) RSM (c) cp along leading-edge

Figure 24: Cp contours on the diamond wing and Cp along the leading edge.

Pressure coefficient distributions delivered by the SA-RC-QCR and RSM are shown in Figure 24. In the case of SA-RC-QCR a shift in the location of suction pressure from the leading edge to the

inboard section of the wing, indicating flow separation, is observed upstream of x/cr = 0.3 whereas in the case of RSM this region is observed directly at x/cr = 0.3.

The cp along the wing leading edge is shown in Figure 24(c). The decrease of the suction pressure indicates the region close to flow separation. As can be seen in the SA-RC-QCR the flow separation from round leading edge occurs earlier than in the RSM. In the pressure contour plots, the extent of suction pressure associated with the outer primary vortex is smaller in the case of RSM compared to the SA-RC-QCR. This is due to the enlarged vortex in the inboard direction and reduced vortex strength in the RSM predictions.

Figure 25 shows the comparison of predicted cp with the experimental data. At the streamwise stations of x/cr = 0.1 and 0.2 the experimental pressure distributions render attached flow. This trend is reproduced in the computations and the predicted pressure is in good agreement with the experiments. At x/c r = 0.295, the experimental cp displays vortex separation by a shift of the suction peak from the leading edge to an inboard location of the wing. In the SA-RC-QCR computation, due to earlier separation, the outer primary vortex is located too far inboard with a higher suction peak compared to the experiments. In the cases of RSM the cp distribution renders attached flow, however a rather slow change in the cp gradient displays that the flow is on the verge of separation.

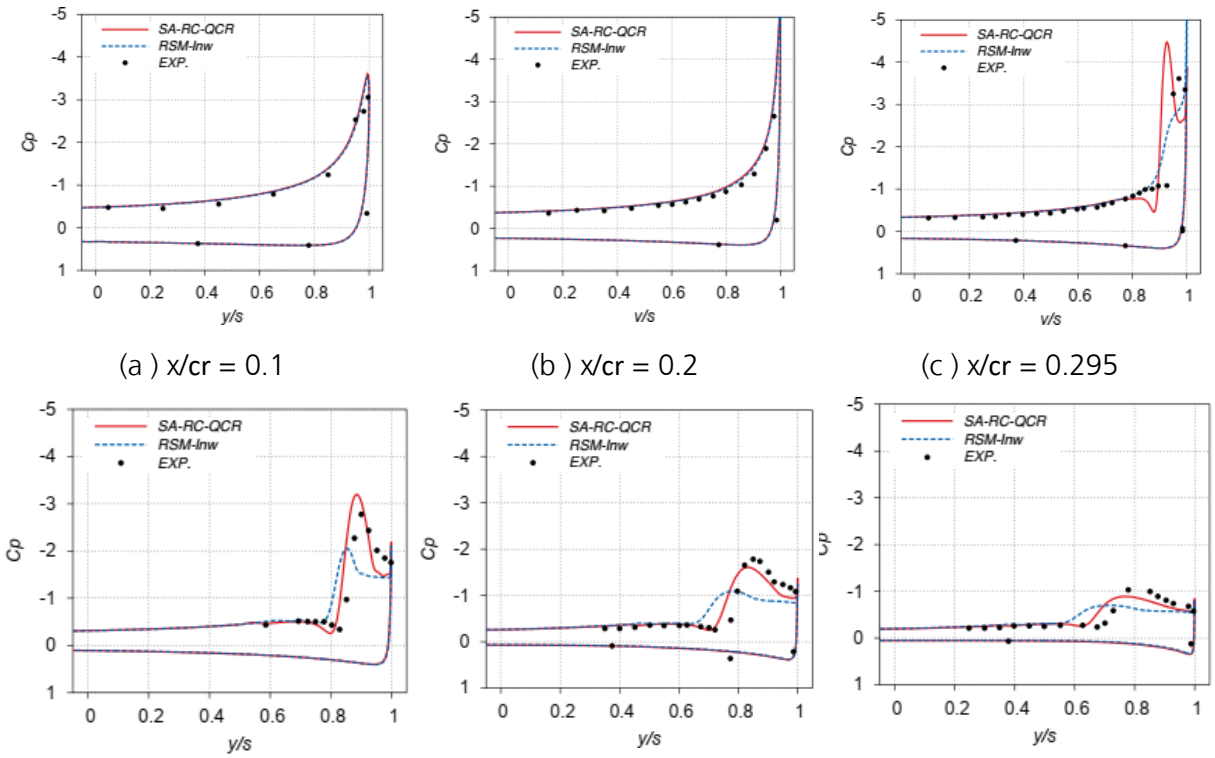

(a) x/cr = 0.1 (b) x/cr = 0.2 (c) x/cr = 0.295

(d) x/cr = 0.395 (e) x/cr = 0.5 (f) x/cr = 0.6

Figure 25: Comparison of Cp distribution on fine grid for delta wing.

At further downstream locations, x/c r = 0.395 to 0.6, a fully developed separated vortex flow trend is observed in the experiments. The local cp peak represents the pressure associated with the vortex. As can be seen in the figure, the pressure associated with the outer primary vortex and its location are well reproduced in the SA-RC-QCR predictions. However, in the RSM investigations, the suction peak associated with the outer primary vortex is underpredicted and its location is delivered more inboard compared to the experiments.

Overall, for this test case, the SA-RC-QCR shows good agreement with experiments with respect to the pressure associated with the outer primary vortex and its location despite earlier separation. Concerning the RSM, though closer agreement with experimental separation location, the downstream development of the vortex is underpredicted.

5.4. Discussion on the performance of RANS models

All the configurations investigated unveil separation from smooth body surface and subsequent formation of vortices. For the spheroid configuration, all the applied RANS models exhibited similar performance—all the models delivered vortices with almost the same strength, which is weaker compared to experiments. For this configuration, RSM has not displayed many improvements compared to the other turbulence models.
For the delta and diamond wing investigations, SST-RC-QCR is not considered for the investigations as it predicts flow separation much too early. For the delta wing, RSM demonstrated improvements with respect to the locations of vortex separation from leading edge and inner primary vortex, which are closer to the experiments.
For the diamond wing, RSM performs poorly by delivering weaker outer primary vortex compared to experiments. For this case, in spite of earlier flow separation, the SA-RC-QCR delivered improved predictions with respect to the downstream development of outer primary vortex.

6. Summary

To evaluate the predictive capabilities of a Reynolds stress model (RSM) for separated vortex flows, investigations are carried out for the flow over a spheroid, a delta wing and a diamond wing. All the cases are characterized by separation from a smooth surface and subsequent vortex formation, the phenomena often observed on military configurations. Here the main objective is to explore the performance of RSM compared to eddy-viscosity models (EVM) and hybrid RANS/LES methods (HRLM) in the prediction of separated vortex flows. To this end, aforementioned configurations are investigated using the SSG/LRR-ln(ω) Reynolds stress model and the predictions are compared to the prediction delivered by EVM and HRLM. In this work, the SA turbulence model coupled with the Rotation/Curvature correction and the Quadratic Constitutive Relation (QCR) are employed as to improve the predictions of the vortices and the normal Reynolds stress anisotropy which exists in the regions of secondary separation. For HRLM, the delayed detached eddy simulation based on SA and SA-RC-QCR are employed.

Prior to the performance studies, grid refinement and grid topology investigations are conducted. After observing grid independence of the predictions, performance studies using, first, RANS models, later HRLM based on EVM, and finally HRLM based on RSM are carried out on appropriate grids.

In the performance study, investigations on the spheroid case unveiled that the predictions delivered by all the applied turbulence models are almost identical, i.e. improvements in the predictions by applying RSM for this case are marginal compared to the other models. Comparing predictions with experiments show that the strength of the primary and secondary vortices still needs to be improved.

For the delta wing, the SA-RC-QCR predicted separation from the leading edge earlier than the one observed in the experiments. This led to an earlier formation of inner and outer primary vortices and an underprediction of the vortex strength and the associated pressure distribution compared to the experiments. In RSM the separation is predicted closer to the experimental separation from the leading edge which lead to improved predictions with respect to the pressure associated with the outer primary vortex. However, the strength of inner primary vortex is underpredicted and its location is more inboard compared to experiments. For this case, still improvements with respect to inner primary vortex strength and location are required.

For the diamond wing, the SA-RC-QCR predicted separation from the leading edge earlier than in the experiments, however, the downstream development of the outer primary vortex is in good agreement with the experiments with regard to the pressure associated with the vortex and its location. In the RSM predictions, vortex separation from leading edge is observed a bit downstream of experimental separation location. Additionally, the primary vortex is enlarged and the pressure

associated with it is overpredicted. Among the applied models, the SA-RC-QCR delivered improved predictions.

Acknowledgements

The research presented in this report was funded by the Air Force office of Scientific Reseach (AFOSR), Award No. FA9550-18-1-7019. The funding is gratefully acknowledged.

References

[1] N. Frink, M. Tomac and A. and Rizzi, "Collaborative study of incipient separation on 53° swept diamond wing," *Aerospace Science and Technology,* vol. 57, pp. 76-89, 2016.

[2] M. Ghoreyshi, K. Ryszka, R. Cummings and A. Lofthouse, "Vortical flow prediction of a diamond wing with rounded leading edges," *AerospaceScienceandTechnology,* pp. vol. 57, pp. 103-117, 2016.

[3] S. Braun, U. A., B. Eisfeld and E. Stumpf, "Numerical Simulation of Vortex Roll-Up Processes Using the SSG/LRR-w," *New Results in Numerical and Experimental Fluid Mechanics X Notes on Numerical Fluid Mechanics and Multidisciplinary Design ,* vol. 132, pp. 481-491, 2016.

[4] V. Togiti, V. Ciobaca, B. Eisfeld and T. Knopp, "Numerical simulation of steady blowing active flow control using a differential reynolds stress model," in *CEAS/KATnet II*, Bremen, Germany, 2009.

[5] T. G. Wetzel, R. L. Simpson and C. J. Chesnakas, "Measurement of three-dimensional crossflow separation," *AIAA Journal,* pp. vol. 36(4), pp. 557-568, 1998.

[6] D. Hummel and G. Redeker, "A new vortex flow experiment for computer code validation," in *RTO-AVT Symposium on Vortex Flow and High Angle of Attack*, Loen, Norway, 7–11 May, 2001.

[7] J. Luckring and D. Hummel, "What was learned from the new VFE-2 experiments," *Aerosp. Sci. Technol.,* vol. 24, no. 1, p. 77–88, 2013.

[8] A. Hövelmann, M. Grawunder, A. Buzica and C. Breitsamter, "AVT-183 diamond wing flow field characteristics Part 2: Experimental analysis of leading-edge vortex formation and progression," *Aerospace Science and Technology,* vol. 57, p. 31–42, 2016.

[9] M. L. Shur, M. K. Strelets, A. K. Travin and P. R. Spalart, "Turbulence Modeling in Rotating and Curved Channels: Assessing the Spalart-Shur Correction," *AIAA journal,* pp. Vol. 38, No. 5, pp. 784-792, 2000.

[10] M. Mani, D. A. Babcock, C. M. Winkler and P. R. and Spalart, "Predictions of a Supersonic Turbulent Flow in a Square Duct," in *AIAA Paper 2013-0860*, 2013.

[11] P. R. Spalart and S. R. Allmaras, " A One-Equation Turbulence Model for Aerodynamic Flows," in *Recherche Aerospatiale*, 1994.

[12] F. R. Menter, "Two-Equation Eddy-Viscosity Turbulence Models for Engineering Applications," *AIAA Journal,* pp. Vol. 32, No. 8, pp. 1598-1605, 1994.

[13] B. Eisfeld, C. Rumsey and V. Togiti, "Verification and Validation of a Second-Moment-Closure Model," *AIAA Journal,* Vols. Vol. 54, No. 5, pp. pp. 1524-1541, 2016.

[14] S. Braun, "Implementation of a ln(w) based SSG/LRR Reynolds Stress Model into the DLR-TAU Code," Institutsbericht, DLR-IB-AS-BS-2019-37, Report of the Institute of Aerodynamics and Flow Technology, Braunschweig, 2019.

[15] D. Schwamborn, T. Gerhold and R. Heinrich, "The DLR TAU-Code: Recent Applications in Research and industry," in *Europen Conference on CFD, ECCOMAS CFD*, 2006.

DLR-IB-AS-BS-2022-62
RANS Investigations of Vortex Separated Flows

V. Togiti, A. Krumbein

Verteiler:

Institutsbibliothek AS	1 Exemplar
Verfasser/Co-Autoren je	1 Exemplar
Institutsleitung	1 Exemplar
Abteilungsleiter	1 Exemplar
Deutsche Bibliothek in Frankfurt/Main	2 Exemplare
Niedersächsische Landesbibliothek Hannover	1 Exemplar
Techn. Informationsbibliothek Hannover	1 Exemplar
Zentralbibliothek BS	1 Exemplar
Zentralarchiv GÖ	1 Exemplar
Reserve	1 Exemplar